

Applications of the National Institute of Standards and Technology (NIST) database for the simulation of electron spectra for surface analysis for quantitative x-ray photoelectron spectroscopy of nanostructures

Cite as: J. Vac. Sci. Technol. A **39**, 063205 (2021); <https://doi.org/10.1116/6.0001261>

Submitted: 05 July 2021 • Accepted: 19 August 2021 • Published Online: 13 September 2021

 Wolfgang S. M. Werner and  Cedric J. Powell

COLLECTIONS

Paper published as part of the special topic on [Commemorating the Career of Charles S. Fadley](#)



View Online



Export Citation



CrossMark

ARTICLES YOU MAY BE INTERESTED IN

[Using the inelastic background in hard x-ray photoelectron spectroscopy for a depth-resolved analysis of the CdS/Cu\(In,Ga\)Se₂ interface](#)

Journal of Vacuum Science & Technology A **39**, 063216 (2021); <https://doi.org/10.1116/6.0001336>

[Innovative remote plasma source for atomic layer deposition for GaN devices](#)

Journal of Vacuum Science & Technology A **39**, 062403 (2021); <https://doi.org/10.1116/6.0001318>

[Low-temperature atomic layer deposition of indium oxide thin films using trimethylindium and oxygen plasma](#)

Journal of Vacuum Science & Technology A **39**, 062406 (2021); <https://doi.org/10.1116/6.0001375>



Instruments for Advanced Science

<ul style="list-style-type: none"> ■ Knowledge, ■ Experience, ■ Expertise <div style="background-color: #c00; color: white; text-align: center; padding: 5px; margin-top: 10px;"> Click to view our product catalogue </div> <p style="font-size: small; margin-top: 10px;">Contact Hiden Analytical for further details: www.HidenAnalytical.com info@hiden.co.uk</p>	<div style="text-align: center;">  <p>Gas Analysis</p> </div> <ul style="list-style-type: none"> ▶ dynamic measurement of reaction gas streams ▶ catalysis and thermal analysis ▶ molecular beam studies ▶ dissolved species probes ▶ fermentation, environmental and ecological studies 	<div style="text-align: center;">  <p>Surface Science</p> </div> <ul style="list-style-type: none"> ▶ UHVTPD ▶ SIMS ▶ end point detection in ion beam etch ▶ elemental imaging - surface mapping 	<div style="text-align: center;">  <p>Plasma Diagnostics</p> </div> <ul style="list-style-type: none"> ▶ plasma source characterization ▶ etch and deposition process reaction kinetic studies ▶ analysis of neutral and radical species
<div style="text-align: center;">  <p>Vacuum Analysis</p> </div> <ul style="list-style-type: none"> ▶ partial pressure measurement and control of process gases ▶ reactive sputter process control ▶ vacuum diagnostics ▶ vacuum coating process monitoring 			

Applications of the National Institute of Standards and Technology (NIST) database for the simulation of electron spectra for surface analysis for quantitative x-ray photoelectron spectroscopy of nanostructures

Cite as: J. Vac. Sci. Technol. A 39, 063205 (2021); doi: 10.1116/6.0001261

Submitted: 5 July 2021 · Accepted: 19 August 2021 ·

Published Online: 13 September 2021



Wolfgang S. M. Werner^{1,a)}  and Cedric J. Powell² 

AFFILIATIONS

¹Institut für Angewandte Physik, Vienna University of Technology, Wiedner Hauptstrasse 8-10, A 1040 Vienna, Austria

²Associate, Materials Measurement Science Division, National Institute of Standards and Technology, Gaithersburg, Maryland 20899-8370

Note: This paper is a part of the Special Collection Commemorating the Career of Charles S. Fadley.

a) Author to whom correspondence should be addressed: werner@iap.tuwien.ac.at

ABSTRACT

SESSA (Simulation of Electron Spectra for Surface Analysis) is a software that was frequently used by the late Charles Fadley, since it provides a convenient means to simulate peak intensities as well as entire spectral regions for photoelectron spectroscopy. X-ray photoelectron spectra can be simulated for several types of nanostructures. SESSA can also be utilized in more complex cases, e.g., if the nondipolar terms in the photoelectric ionization cross section need to be taken into account, a typical situation encountered in spectroscopy using synchrotron radiation. The software was initially released in 2005 as a National Institute of Standards and Technology Standard Reference Database. Here, we describe two new features that have recently been added to the newest version (SESSA V2.2) of the software, i.e., simulation of surface excitations and an effective approach to account for the energy dependence of the interaction characteristics of emitted photoelectrons. Furthermore, we illustrate some functionalities of SESSA by presenting several applications. These include overlayer measurements to determine the effective electron attenuation length, quantitative analysis of impurities in multilayer materials, analysis of ionic liquids, the influence of nondipolar effects for photon energies above a few keV, and analysis of nanoparticles by means of photoelectron spectroscopy.

© 2021 Author(s). All article content, except where otherwise noted, is licensed under a Creative Commons Attribution (CC BY) license (<http://creativecommons.org/licenses/by/4.0/>). <https://doi.org/10.1116/6.0001261>

I. INTRODUCTION

The late Charles (Chuck) Fadley published a large number of papers that described applications of x-ray photoelectron spectroscopy (XPS) to a wide range of advanced materials. In recent years, these investigations included studies of the electronic structure of the dilute magnetic semiconductor $\text{Ga}_{1-x}\text{Mn}_x\text{P}$ with so-called hard XPS (also known as HAXPES),¹ characterization of free-standing InAs quantum membranes by standing-wave HAXPES,² unexpected termination switching and polarity compensation in $\text{LaAlO}_3/\text{SrTiO}_3$ heterostructures,³ and structural studies of an epitaxial Fe/MgO

multilayer magnetic tunnel junction with standing-wave HAXPES.⁴ These investigations were aided by the use of the National Institute of Standards and Technology (NIST) Database for the Simulation of Electron Spectra for Surface Analysis (SESSA).^{5,6}

SESSA can be used to simulate XPS spectra of multilayer films as well as nanostructures such as islands, lines, spheres, and layered spheres on surfaces. As for earlier versions, such simulations can be performed for multilayer films. Users can specify the compositions and dimensions of each material in the sample structure as well as the measurement configuration. SESSA contains the physical data

needed to perform quantitative interpretation of an XPS spectrum for a specimen of given composition and morphology. XPS spectra can be simulated for the specified sample structure and measurement conditions, and the simulated spectra can be compared with measured spectra. Compositions and dimensions can then be adjusted to find maximum consistency between simulated and measured spectra.

In this paper, we outline the structure and operation of the software and briefly describe newer features of SESSA that have been added since its release in 2005.⁷ Owing to the very general structure of the SESSA software, it can be used for a large range of analytical applications involving XPS intensities and spectral shapes. The accuracy with which SESSA can be used to quantitatively predict XPS signal intensities has been tested in various ways by comparing results of SESSA simulations with different models specifically developed for a given problem. In Sec. III, we present examples of SESSA that illustrate how it can be utilized for various tasks involved in quantifying XPS intensities.

II. FUNCTIONALITIES OF SESSA

SESSA contains physical data needed to perform quantitative interpretation of an XPS spectrum or an Auger-electron spectrum (AES) for a specimen of given composition and morphology (differential inverse inelastic mean free paths (IMFPs), total inelastic mean free paths, differential elastic-scattering cross sections, total elastic-scattering cross sections, transport cross sections, photoionization cross sections, photoionization asymmetry parameters, electron-impact ionization cross sections, photoelectron line shapes, Auger-electron line shapes, fluorescence yields, and Auger-electron backscattering factors). Retrieval of relevant data is performed by a small expert system that queries the comprehensive databases. A simulation module provides an estimate of peak intensities as well as the peak spectra. A user can select data values from two or more databases for each parameter or even, if desired, insert their own values. Users can also choose a particular function (Lorentzian, Gaussian, or Doniach–Sunjic) to describe the intrinsic shape of a photoelectron line. There is also an “Empirical” option with which a text file can be entered into SESSA that could, for example, be an experimental line shape or the line shape from a function that was considered to be appropriate for a particular peak.⁸

The design of the SESSA software allows the user to enter the required information in a reasonably simple way. The modular structure of the user interface closely matches that of the usual control units on a real instrument. Any user who is familiar with a typical XPS spectrometer can perform a retrieval/simulation operation with the SESSA software in a few minutes for a specimen with a given composition and morphology. A command line interface can also control the software; this feature allows users to load sequences of commands that facilitate simulations for similar conditions.

SESSA was initially designed to simulate XPS and AES spectra from multilayer thin-film structures. Users could specify the compositions and dimensions of each material in the structure as well as the measurement configuration, and the simulated spectra could be compared with measured spectra. The simulation of electron spectra in SESSA employs the trajectory-reversal Monte Carlo method,⁹ making it highly efficient: simulation of a full spectrum typically takes a fraction of a second on a modern personal computer.

Since the release of Version 1 of SESSA in 2005,⁵ later versions have incorporated additional data and capabilities. These enhancements have included the ability to perform simulations with polarized x rays and to make these simulations with nondipole photoionization cross sections. The former improvement is necessary for simulations relevant to XPS at synchrotron light sources while the latter is required for simulations with x-ray energies larger than about 2 keV.

Version 2.0 of SESSA¹⁰ was released in 2014 with additional capabilities for specifying specimen nanomorphologies (such as islands, lines, spheres, and layered spheres on surfaces). This version allows users to create new sample morphologies with the PENGEO geometry package.¹¹ For this and subsequent releases, additional databases have been added for inelastic mean free paths and for electron-impact ionization cross sections. Version 2.2 was released in March 2021.¹² It contains a new database for inelastic mean free paths and the two new functionalities described below.

A. Modeling surface excitations

A simple model for surface excitations induced by Auger or photoelectrons escaping from semi-infinite solids with planar surfaces and energy losses suffered as a consequence has been implemented in SESSA.^{13,14} Surface excitations are additional modes of the inelastic-scattering process in the bulk of a material and are a consequence of the boundary conditions of Maxwell’s equations near an interface between media with different dielectric constants, in the present case the sample and the vacuum. The starting point of this model is the so-called partial intensity approach based on the contribution of the spectrum of electrons that have participated a certain number of times in specific scattering processes.¹⁵ The depth range where surface excitations take place is very shallow inside the solid, although surface excitations also take place in vacuum when the probing electron still interacts with the solid-state electrons. When the path length of escaping electrons inside the surface-scattering zone is sufficiently small compared to the characteristic mean free path for deflections, the passage through the surface-scattering zone is approximately rectilinear, and the partial intensities for bulk and surface scattering are uncorrelated,^{13,16,17}

$$C_{n_b, n_s} = C_{n_b} \times C_{n_s}, \quad (1)$$

where n_b and n_s are the collision numbers for bulk and surface scattering, respectively. Rectilinear passage also implies that the probability for plural surface scattering is governed by the Poisson stochastic process,

$$C_{n_s}(E, \theta) = \frac{\langle n_s(E, \theta) \rangle^{n_s}}{n_s!} e^{-\langle n_s(E, \theta) \rangle}, \quad (2)$$

where $\langle n_s(E, \theta) \rangle$ is the average number of surface excitations during a single surface crossing with energy E and angle θ (with respect to the surface normal). Different physical models have been proposed in the literature for the average number of surface excitations, qualitatively expressing the fact that $\langle n_s(E, \theta) \rangle$ should roughly be proportional to the time the electron spends in the surface-scattering zone. The result by Oswald,¹⁸ based on the work

of Stern and Ferrell¹⁹ is given as

$$\langle n_s(E, \theta) \rangle = \frac{1}{a_{DB} \sqrt{E \cos \theta} + 1}. \quad (3)$$

An alternative mathematical form for $\langle n_s(E, \theta) \rangle$ is^{20,21}

$$\langle n_s(E, \theta) \rangle = \frac{1}{a_{DB} \sqrt{E \cos \theta}}. \quad (4)$$

Note that the material parameter a_{DB} in Eq. (4) is generally defined differently in the literature. Here the reciprocal value is used to ensure consistency with Eq. (3). Following the convention in the literature,¹⁴ the quantity a_{DB} will be referred to as the “surface excitation parameter” (SEP) in the following. Databases for the SEP have been implemented in SESSA from which the average number of surface excitations is calculated as indicated in Table I.

Concerning the reliability of the databases available within SESSA for a specific material, the use of the empirical databases is recommended (SEP01 or SEP02). If a datum is available for the material in question this has been proven to describe corresponding electron energy loss spectra quantitatively. Alternatively, it is recommended to use the empirical formula (SEP03), which can be used as a guide for calculating values of the SEP. The above choices are generally expected to be more realistic than the estimates for nearly free-electron materials (SEP04 and SEP05).

In analogy to the case of bulk excitations (see, e.g., Ref. 22), the distribution of energy losses T in a single surface excitation, $w_s(T)$, the so-called differential surface excitation parameter is introduced. To account for the passage through the surface scattering zone, the spectrum $Y(E, \theta)$ in the partial intensity approach is given by

$$Y(E, \theta) = \sum_{n_s=0}^{N_{max}} C_{n_s}(E, \theta) \int_0^\infty Y_{Bulk}(E + T, \theta) L_{n_s}(T) dT, \quad (5)$$

where $Y_{Bulk}(E, \theta)$ is the bulk spectrum and the partial loss distributions for surface excitations $L_{n_s}(T)$ are calculated from a self-convolution of $w_s(T)$, and N_{max} is the maximum number of surface

TABLE I. Summary of databases in SESSA for the surface excitation parameter (SEP) and employed equation used in conjunction to calculate the average number of surface excitations (Refs. 14, 18, 20, and 21). The quantity $\hbar\omega_p$ is the universal guideline to calculate the SEP in Ref. 14 is the plasmon energy, which is calculated in SESSA from the density of the material, a_0 is the Bohr radius, and e the elementary charge. The column headed #SE Al2p shows the average number of surface excitations retrieved from the corresponding SEP databases for the spectra shown in Fig. 1.

Name	Equation	SEP(a_{DB})	#SE for Al2p	Reference
SEP01	(3)	Empirical	0.121	14
SEP02	(4)	Empirical	0.243	20
SEP03	(3)	$0.039\hbar\omega_p + 0.4$	0.175	14
SEP04	(4)	$\sqrt{32a_0e^2/\pi^2}$	0.345	21
SEP05	(3)	$\sqrt{8a_0/\pi^2e^2}$	0.173	18

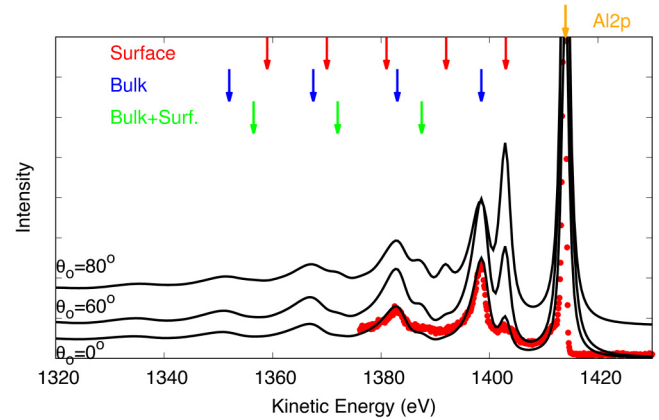


FIG. 1. SESSA simulated Al-Kα XPS spectrum of the Al 2p peak for a homogeneous Al sample, illustrating the model for surface excitations. Curves: SESSA simulations and data points: experimental Al2p spectrum at normal emission normalized to the simulated intensity of the (no-loss) photopeak (see text).

excitations which is considered (usually $N_{max} = 2$ to 5 represents a good choice).

An example of the application of the above algorithm to account for surface excitations of electrons escaping from flat planar surfaces is shown in Fig. 1. The result shows the simulated Al-Kα excited XPS spectrum of the Al 2p-photoelectron peak for several different emission angles using the database SEP03. It is seen that in addition to the bulk plasmon replicas of the main photoelectron peak (arrows labeled “Bulk”), surface plasmon replicas also appear, although only the first two are appreciable in size (those at energies of ≈ 1403 and 1392 eV, the first two arrows labeled “Surface” left of the main peak) since higher-order surface partial intensities decrease rapidly by virtue of the Poisson stochastic process when $\langle n_s(E, \theta) \rangle < 1$ [see Eq. (2)]. The bulk plasmons themselves are also replicated by the surface plasmons as indicated by the green arrows, reflecting the fact that the partial intensities $C_{n_b, n_s=1}$ always assume appreciable values, while for $n_s \geq 2$ surface excitations are practically negligible.

The data points show an experimental Al 2p spectrum recorded at normal emission. The simulated spectrum was normalized to the experimental spectrum so that the areas of the main Al 2p peak were the same. Both the shape and the intensity of the sequence of surface plasmons as well as the mixed surface and bulk plasmon excitations (green arrows) are reasonably reproduced by the simulation.

B. Spectrum modeling beyond the quasielastic approximation

The main interest in simulating XPS data is usually concerned either with peak intensities for the purpose of quantitation of experimental spectra or the inelastic background in the vicinity of a peak. This is the reason why in the literature, the quasielastic approximation (QEA) is commonly invoked, where it is assumed that the interaction characteristics (for energies not too far away

from the photopeak) do not depend on the energy. In the present context, the term “interaction parameters” mainly refers to the IMFP and the elastic-scattering cross section. This approximation yields the exact result for the zero-loss peak, often referred to as the elastic peak or simply the photoelectron “peak.” If a significant energy loss range is of interest, as, for example, for inelastic-background analysis to obtain information about the sample morphology, the quasielastic approximation may become invalid and it would be desirable to account for the energy dependence of the interaction characteristics in the simulation in some way. In principle, this can be achieved by employing the so-called direct simulation approach in a Monte Carlo simulation.²³ However, this procedure comes at the cost of increased complexity and a severe decrease in computational efficiency, and, moreover, it is strictly impossible to combine a direct simulation approach with the trajectory-reversal algorithm since the latter is based on Case’s reciprocity theorem for *one speed* transport.²⁴

A simple and effective workaround has been proposed in Ref. 25. There, it is observed that the partial intensity approach is conceptually similar to the multispeed approximation employed in

the numerical solution of the transport equation in neutron physics,²⁶ in which the particle flux is divided into groups within a certain speed interval. In a statistical sense, the n th order partial intensities correspond to the group of particles within a certain speed range. Since their intensity is governed by the Poisson distribution after n collisions [see Eq. (8)] and, therefore, by the inelastic mean free path after n inelastic collisions, a simple, yet effective, way to account for the energy dependence of the interaction characteristics is to multiply the peak spectrum $Y_{\text{QEA}}(E)$ by the energy dependence of the inelastic mean free path,

$$Y_{\text{QEA}^+}(E) = Y_{\text{QEA}}(E) \times \frac{\lambda(E)}{\lambda(E_0)}, \quad (6)$$

where $\lambda(E)$ is the IMFP for energy E and $\lambda(E_0)$ is the IMFP for energy E_0 of the photoelectron peak. We refer to this procedure as the QEA^+ -approximation.

One of the underlying implications of this type of approximation is that the energy dependence of the elastic interaction is negligible. For sufficiently smooth initial angular distributions at the source, where the photoionization takes place, the so-called generalized radiative field similarity principle²⁷ states that the details of the elastic cross section do not essentially affect the path length distribution and hence the partial intensities will mainly change due to the energy dependence of the inelastic mean free path, which is approximately accounted for by Eq. (6). Indeed the distribution of path lengths for Auger- or photoelectrons is not significantly affected by the energy dependence of the elastic-scattering cross section. This makes the QEA^+ -approximation an effective approach in true slowing down problems even for a sharply peaked initial angular distribution, such as for reflection of a focused beam of electrons from a surface.²⁸

A comparison between the QEA (curve labeled QEA) and QEA^+ (curve labeled QEA^+) approximation is shown in Fig. 2. Panel (a) represents the case of a homogeneous Al sample, while in panel (b) the resulting simulated spectra for a core-shell nanoparticle with a 12 nm gold core and a 1 nm silver shell are shown. The employed nanoparticle is schematically illustrated in panel (b). The curve labeled “QEA” in panel (b) represents the quasielastic approximation (QEA) while the curve labeled QEA^+ is the QEA^+ -approximation [Eq. (6)] and the curve labeled “SDN” is the true slowing down (SDN) Monte Carlo calculation, which is the most realistic.²⁵ It is seen that the quasielastic approximation is satisfactory for energy losses ΔE less than about 10% of the initial energy and the effect of the change in the interaction characteristics becomes noticeable only if a broader energy range is considered.

III. APPLICATIONS

A. Attenuation length measurements over a wide energy range using the overlayer method

Our first example of an application of SESA concerns measurements of effective attenuation lengths (EALs) for the measurement of overlayer-film thicknesses, L_{TH} , by XPS. In the early days of XPS, many measurements were made of these EALs to obtain measures of the surface sensitivity of XPS.^{29–32} At this time (prior to 1980), the effects of elastic scattering of photoelectrons had not

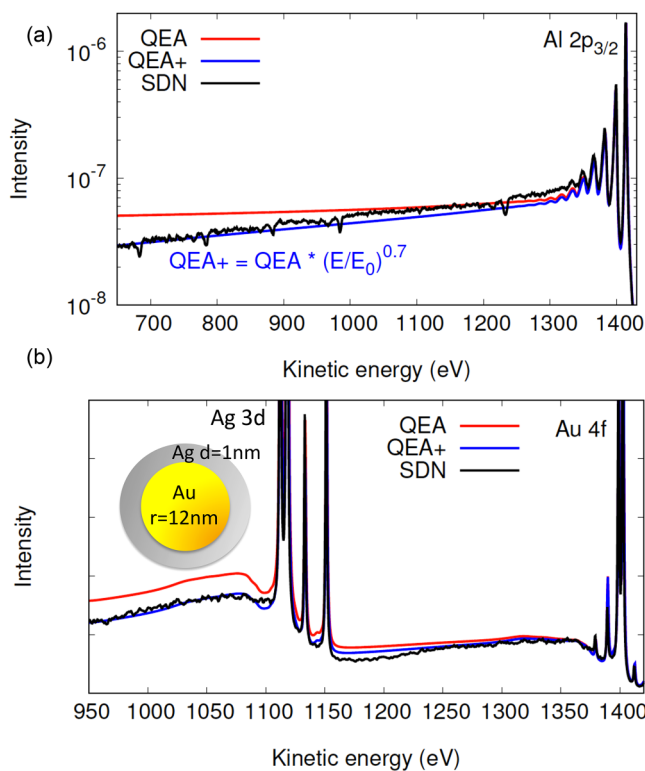


FIG. 2. Comparison of the QEA^+ approximation to account for the variation of the interaction characteristics with energy. (a) For a homogeneous Al sample and (b) for a core-shell nanoparticle with a 12 nm gold core and a 1 nm silver shell, schematically illustrated in the inset. Solid curve labeled “QEA”: quasielastic approximation; solid curve labeled “ QEA^+ ”: QEA^+ -approximation [Eq. (6)]; and solid curve labeled “SDN”: SDN Monte Carlo calculation (Ref. 25).

been recognized, and it was commonplace then to refer to the measured quantities as attenuation lengths, IMFPs, and escape depths. Each of these terms now has a separate meaning and definition.³³

EAL measurements were typically made by depositing an overlayer film on a substrate material and measuring changes in the intensities of photoelectron signals from the film and substrate materials as a function of film thickness. A number of simplifying assumptions were made in conducting these experiments and in interpreting the results.³³ One major assumption was that the overlayer film was homogeneous and of uniform thickness. Although no direct assessments could then be made of film uniformity, it was assumed that exponential increases or decreases of signal intensities with increasing film thickness were reliable indications of film uniformity. Similarly, deviations from exponential dependencies were indications that the film was not uniform, and the results were typically discarded.

We will now summarize an analysis of EAL measurements for gold by Rubio-Zuazo and Castro (RZC)³⁴ that were made by depositing thin films of gold on a polycrystalline copper substrate.³⁵ They measured the intensities of various Cu and Au photoelectron lines as a function of Au film thickness in XPS experiments at a synchrotron light source. RZC found exponential decreases of the Cu photoelectron intensities and exponential increases of the Au photoelectron intensities with increasing Au film thickness. The symbols in Fig. 3 show nine EALs for Au and their estimated

uncertainties for photoelectron energies between 1029 and 9694 eV. The RZC experiments are noteworthy in that EALs were determined over a wide energy range and that x-ray reflectivity (XRR) measurements on their sample could be performed during deposition of the Au films and without moving the Cu substrate from the XPS analysis position. Analysis of the XRR data yielded the film thickness with an accuracy better than 1% of the film thickness and the RMS roughness with an accuracy better than 10% of the roughness value.³⁴

The dashed line in Fig. 3 shows IMFPs for Au from the calculations of Tanuma *et al.*³⁶ and the solid line shows the predicted EALs from Jablonski's predictive EAL formula for linearly polarized x rays,³⁷

$$L_{TH} = \lambda_i(1 - 0.836\omega), \quad (7)$$

where λ_i is the IMFP for Au and ω is the single-scattering albedo for Au. The latter parameter is a useful measure of the strength of elastic-scattering effects on photoelectron trajectories.^{22,27,33} The five EALs in Fig. 3 for energies between 8752 and 9694 eV are less than the corresponding IMFPs, as expected, and are also close to values expected from Eq. (7). However, the four EALs at lower energies are larger than the predicted values, and two of the EAL values, for energies of 1029 and 2921 eV, are larger than the calculated IMFPs. While it is possible that the calculated IMFPs for Au could be incorrect, these values are consistent with other IMFP calculations and measurements.

Powell and Jablonski (PJ)³⁵ have recently reinterpreted the RZC experiments.³⁴ RZC derived their EALs with the assumption that their Au films were of uniform thickness (i.e., Frank-van der Merwe or layer-by-layer film growth). PJ considered two other forms of film growth: island formation (Volmer-Weber film growth) and island growth on a continuous monatomic Au wetting layer (Stranski-Krastanov film growth). Simulations were made with Version 2.1.1 of the NIST *SESSA* database and the islands morphology⁷ to find relative Au island areas for each Au film thickness that matched the exponential intensity changes reported by RZC.

In *SESSA*, islands are represented as two-dimensional periodic arrays with periodicities X and Y . For simplicity, PJ chose $X = Y = 1000$ nm although their results were not sensitive to this choice. For each Au island height (corresponding to the Au film thickness in the RZC experiments), PJ found the dimensions (x , y) of an assumed square Au island that yielded a Cu 1s, Cu 2s, or Au 3s photoelectron intensity that matched the corresponding exponential decrease (for the Cu signals) or exponential increase (for the Au signal) found in the RZC experiments within 1%. They could then determine the relative Au island areas (xy/XY) for each Au film thickness.

Figure 4 shows a comparison of relative Au island areas as a function of Au film thickness for Volmer-Weber film growth (no wetting layer) and Stranski-Krastanov film growth (Au wetting layer). These comparisons were made, for example, for photoelectron energies of (a) 1029 and (b) 6583 eV. We show uncertainties in some points based on the results of *SESSA* simulations in which relative Au island areas were determined for $\pm 5\%$ variations in the calculated IMFPs of Tanuma *et al.* We see consistent results for growth in the relative Au island areas for the two photoelectron

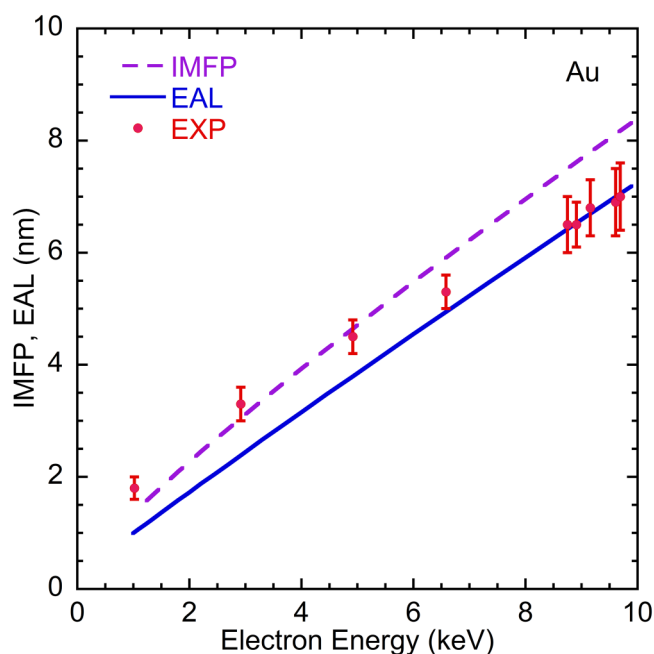


FIG. 3. Dependence of the IMFP and the EAL for Au on photoelectron kinetic energy (Ref. 36). Solid line: Jablonski's predictive EAL formula for polarized x rays [Eq. (7)] and dashed line: calculated IMFPs from Tanuma *et al.* (Ref. 36). Symbols indicate experimentally determined EALs and their uncertainties (Ref. 34).

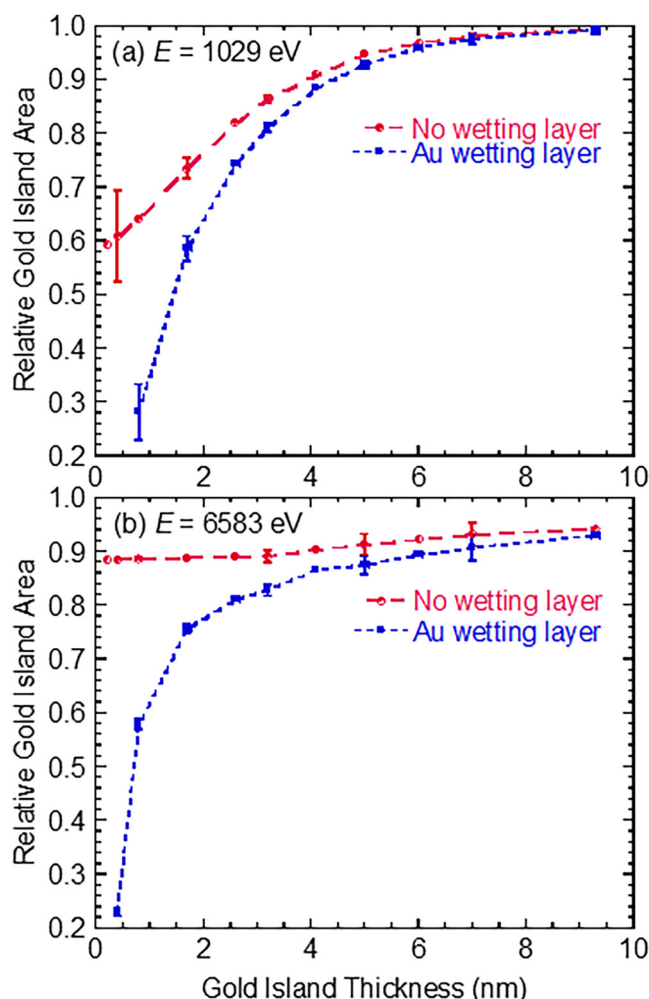


FIG. 4. Comparisons of relative gold island areas as a function of gold island thickness for Volmer-Weber film growth (no wetting layer) and for Stranski-Krastanov film growth (Au wetting layer) for photoelectron energies, E , of (a) 1029 and (b) 6583 eV (Ref. 35). Uncertainties are indicated for some points based on assumed uncertainties of $\pm 5\%$ in the calculated IMFPs of Tanuma *et al.* (Ref. 36). Lines are shown between points to guide the eye.

energies from the simulations with an Au wetting layer. No such consistency is found for the simulations without a wetting layer. An important conclusion of this work is that the exponential growth of overlayer intensity or decay of substrate intensity with increasing overlayer-film thickness does not necessarily mean that the film is uniform.

We note that the analysis of the RZC experiments with *SESSA* (Ref. 35) was based on the assumptions that the Au islands were square and had rectangular edges. While these assumptions are clearly unrealistic, there appears to be an adequate qualitative agreement between the gold island growth curves in Fig. 4 for photoelectron energies of 1029 and 6583 eV and the assumed

Stranski-Krastanov film growth with a monatomic Au wetting layer. We also point out that the RZC measurements of EALs at the higher energies in Fig. 3 (where the EALs are over 6 nm) are less sensitive to overlayer-film nonuniformities than the EAL measurements at lower energies, where the reported EAL at 1.029 keV was 1.8 ± 0.2 nm. At the higher energies, thicker overlayer films would be utilized in the experiments, and full or partial coalescence of any islands would be more likely.

We also point out that RZC fitted their measured EALs to the empirical relation $L_{TH} = kE^p$, where the EALs are expressed in nm and the photoelectron energy, E , is in eV. They found $k = 0.023 \pm 0.002$ and $p = 0.62 \pm 0.01$ where the uncertainties indicate the standard deviations for each parameter from their fits. In contrast, Powell^{38,39} found that the value of p from Au EALs calculated from Eq. (7) for electron energies between 992.3 and 19.33 keV was 0.871 ± 0.003 . We believe that the smaller value of the parameter p for Au from the RZC experiments (0.62 ± 0.01) than the calculated value (0.871 ± 0.003) is another indication of the effects of islanding in the early stages of film growth in the RZC work and in many EAL measurements for other materials.⁴⁰

In this example, *SESSA* simulations with the islands morphology⁷ provided important new information from the careful RZC experiments. It was shown that exponential changes in photoelectron intensities during the growth of an overlayer film on a planar substrate did not necessarily mean that the film was uniform. The simulations showed that the observed intensity changes could be interpreted in terms of Stranski-Krastanov film growth, a much more common form of film growth than layer-by-layer growth.^{41,42}

Jablonski and Powell have recently published a comprehensive review of EALs for different quantitative applications of XPS.³³ They point out that EALs can be defined for different XPS applications (e.g., measurement of film thicknesses on a planar substrate, quantitative analyses, marker depths, and shell thicknesses of nanospheres) and that EALs for one application and instrument configuration can be numerically different from those for another. In addition, EALs for the measurement of film thicknesses for XPS with linearly polarized x rays can be different from those with unpolarized x rays.

B. Quantitative analysis of surface impurities on multilayered materials

Quantitative analyses by XPS are often based on the implicit assumption that the sample of interest is homogeneous over the sampling volume of the XPS measurement. The observed intensities of photoelectron peaks are then analyzed with relative sensitivity factors to obtain a sample composition. However, many samples of interest are inhomogeneous, either laterally or with depth (or both). Tougaard has developed algorithms and software that have been effective in identifying such inhomogeneities and in obtaining quantitative information about inhomogeneous samples from XPS measurements.⁴³

SESSA is also useful for identifying sample inhomogeneities and in obtaining quantitative information about an inhomogeneous sample. We now describe an application in which *SESSA* was used to determine absolute amounts of low-level surface impurities on layered samples of the type used for extreme ultraviolet (EUV)

lithography.⁴⁴ In this application, it was possible to estimate the total uncertainty of such measurements by considering the systematic limitations of *SESSA* and the statistical uncertainties of the measurements. The same procedure can be employed for other multilayered materials.

Faradzhev *et al.*⁴⁴ compared measured and simulated XPS spectra of a witness sample of a type used for EUV resist-outgassing tests. High fluxes of energetic EUV photons (with a wavelength of 13.5 nm) combined with the outgassing from resists can damage EUV optics.⁴⁵ Figure 5 is a schematic diagram of the witness samples used for the investigations with *SESSA*. About 50 Si (4.3 nm)/Mo (3 nm) bilayers were deposited on an Si substrate. The top bilayer was coated with a polycrystalline Ru capping layer of about 3 nm thickness. This film has a native oxide ($\text{RuO}_{x \approx 2}$) layer with a thickness of about 0.5 nm. One or more trace elements (such as F, Cl, Br, N, S, or P) could be detected on particular samples and covered with a thin hydrocarbon layer resulting from air exposure. The latter layer was simulated as carbon that could contain the trace elements. In the XPS measurements for the particular sample of interest here, a weak Cl impurity peak was detected and stronger O and Si peaks that were believed due to oxidized silicon dust particles produced when the samples were cut from a larger wafer. It was, therefore, decided to include an outermost 0.25 nm layer of SiO_2 in the *SESSA* simulations.

Details of the simulations are given in the original report.⁴⁴ We note here that photoelectron peak shapes were assumed to be Lorentzian in the simulations. The widths of the major peaks in the simulated spectra were adjusted to correspond to those in the measured spectra. The simulations were performed with a single differential inelastic mean free path (appropriate for Ru) that does not provide a good match with the energy-loss features on the low-kinetic-energy side of each photoelectron peak in Fig. 6.

The solid (blue) circles in Fig. 6 show the wide-scan spectrum for the witness sample that was measured with a commercial XPS instrument and Al $K\alpha$ x rays.⁴⁴ The solid (red) triangles show a simulated spectrum for the same XPS measurement conditions and a sample consisting of a 0.25 nm layer of SiO_2 on 0.25 nm $\text{CCl}_{0.01}$, 0.25 nm C, 0.25 nm RuO_2 , 3 nm Ru, 4.3 nm Si, and 3 nm Mo on an Si substrate. It was not necessary to include additional Si/Mo bilayers in the simulations because of the limited information

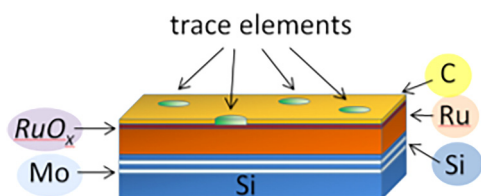


FIG. 5. Sketch of surface model of multilayer mirror used in *SESSA* simulations of trace elements (Ref. 44): Mo/Si bilayers deposited on an Si substrate and coated with an Ru polycrystalline film. This film has a native oxide ($\text{RuO}_{x \approx 2}$) with a thickness of 0.5 nm. One or more trace elements are located on top of this oxide film and covered with a thin hydrocarbon layer resulting from air exposure (simulated by a thin layer of carbon). Reproduced with permission from Faradzhev *et al.*, *Surf. Interface Anal.* **49**, 1214–1224. Copyright 2017, Wiley.

depth of the XPS measurements. The simulated spectrum was multiplied by the transmission function of the XPS instrument and normalized to the measured spectrum at a binding energy of 400 eV.

The measured and simulated spectra in Fig. 6 are qualitatively similar but there are differences in the heights and shapes of the Ru peaks. The weak Cl 2p peak occurs on a background due to the other elements in the sample. However, the intensity of the simulated Cl 2p peak did not vary significantly with changes in the C, RuO_2 , and Ru film thicknesses. We note that we only need rough matches of the peak intensities and inelastic backgrounds in Fig. 6 to quantify the amount of Cl in the sample. Furthermore, we point out that the absence of structure on the low-kinetic-energy side of the Cl peak in a separate narrow scan of this peak (not shown) indicates that the Cl is a surface or near-surface impurity. We also

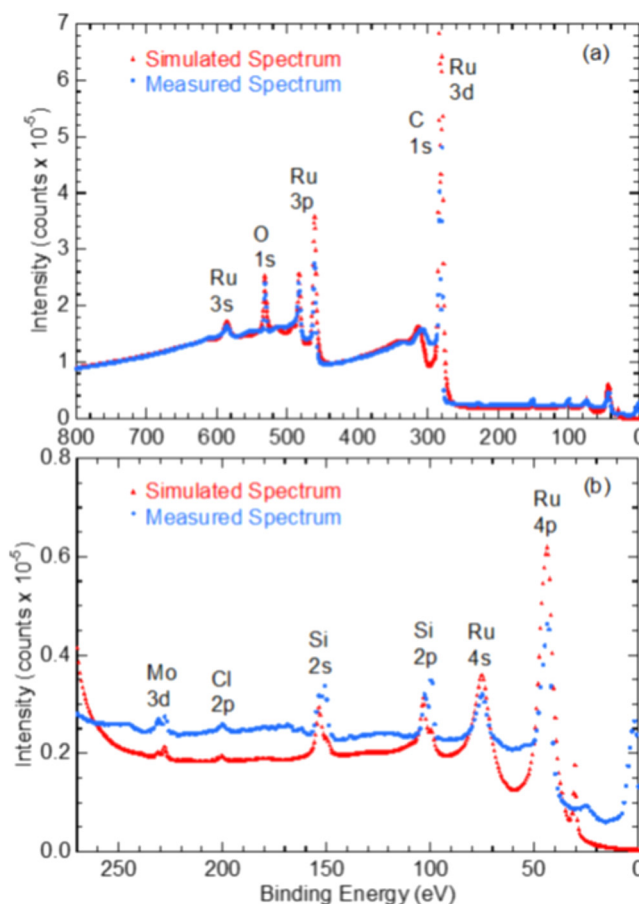


FIG. 6. (a) Comparison of measured (solid circles, blue) and simulated (solid triangles, red) XPS spectra for a multilayer mirror witness sample (Ref. 44). The ordinate scale is the total number of measured photoelectrons at each energy. The simulated spectrum was normalized to the measured spectrum at a binding energy of 400 eV. (b) Expanded low-binding-energy region of (a). Reproduced with permission from Faradzhev *et al.*, *Surf. Interface Anal.* **49**, 1214–1224. Copyright 2017, Wiley.

note that SESSA does not simulate valence-band spectra and the inelastic backgrounds associated with valence-band photoemission. While the agreement between measured and simulated spectra in Fig. 6 could possibly be improved, the main goal of the work was in the relative magnitudes of the Cl 2p peaks above their local backgrounds in the measured and simulated spectra.

Comparison of the background-subtracted Cl 2p peak areas in the simulated and measured narrow-scan spectra indicated that the composition of the outermost 0.25 nm carbonaceous layer was $\text{CCl}_{0.027}$. This composition corresponds to a Cl coverage of 0.020 monolayers assuming a van der Waals radius for Cl of 0.175 nm. The relative statistical uncertainty of this result was estimated to be 13%. The systematic uncertainty of the Cl 2p photoionization cross section was estimated to be about 9% and the uncertainty associated with the neglect of surface and shakeup excitations was estimated to be about 13%. The combined one-standard-deviation systematic uncertainty is then 16% and the total uncertainty in the amount of surface Cl is 21%.

C. Analysis of ionic liquids for determination of the analyzer transmission function

An example of a comparison of SESSA with other available models concerns the analysis of ionic liquids (ILs), which are very suitable materials for performing a relatively easy calibration of the transmission function of the analyzer of an XPS instrument. Ionic liquids are easy to prepare by casting a drop on a sample holder, they have a very low vapor pressure, so these materials are fully UHV-compatible, they are conductive, unaltered after x-ray exposure, and exhibit well separated photoemission peaks covering the main energy range of interest for XPS. ILs can be easily prepared to exhibit a flat surface almost free of adventitious carbon contamination (and time-consuming sputtering and annealing cycles as needed for metallic reference materials can be omitted) and ILs are sufficiently homogeneous both in-depth as well as laterally. Finally, nonfunctionalized ILs are inert to surface oxidation.

The potential of ionic liquids for the use as reference material for the calibration of the spectrometer transmission function of XPS instruments has been recently studied by Holzweber *et al.*⁴⁶ These authors studied the class of 1,3-dialkylimidazolium ionic liquids with bis(tri-fluoromethylsulfonyl)imide as counterion, $[\text{C}_n\text{C}_1\text{im}][\text{NTf}_2]$ (see Fig. 7), for different values of n . These multi-elemental samples exhibit five intensive photoemission peaks, F1s, O1s, N1s, C1s, and S2p, in an energy window from 160 to 700 eV on the binding energy scale. This range is the most important for applications of quantitative XPS for surface chemical analysis of soft matter. Spectra of these ILs were recorded at different laboratories with different instruments and were quantified with the UNIFIT software^{47,48} to yield the transmission function of the respective instruments. It was found that the ILs for $n = 2, 3$, i.e., the ionic liquids with an ethyl or propyl-group are best suited as reference materials. The reason is that these ionic liquids are homogeneous within the information depth of XPS. Peak intensities after calibration of the transmission function were then compared with SESSA simulations. The comparison is shown in Fig. 7 for the carbon, oxygen, nitrogen, and sulfur signals, normalized by the F1s-signal. An almost perfect correlation between the experimental intensities,

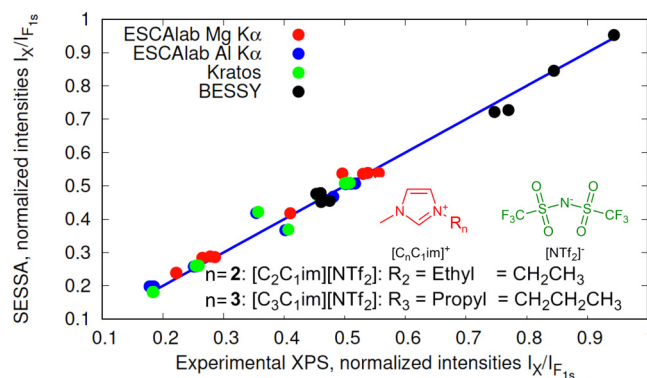


FIG. 7. Intensities of carbon, oxygen, nitrogen, and sulfur signals, normalized by the F1s signal measured on an ionic liquid for determination of the spectrometer transmission function (Ref. 46). The horizontal scale represents experimental peak intensities measured on different instruments corrected for the transmission function of the analyzer using the UNIFIT software (Refs. 47 and 48), and the vertical axis represents corresponding intensities (normalized by the F1s signal) obtained by SESSA. The straight line has a unity slope and passes through the origin, and the data points show evaluations of data from different laboratories, as indicated in the legend (Ref. 46).

shown on the horizontal axis and SESSA (vertical axis), results, which, while being gratifying, may be surprising at first sight since SESSA is based on a more general approach than the UNIFIT software and specifically accounts for elastic scattering, while it is neglected in the UNIFIT software.

However, it is well known that for organic materials, the effect of elastic scattering on XPS intensities is rather weak. These materials consist of atoms with low atomic number and hence the screened Coulomb potential of the ionic cores, which is mainly responsible for changes in the electron direction of motion, is rather weak. This situation implies that the momentum transfer in an elastic collision is generally small, on average leading to small deflection angles. The characteristic path length measuring the momentum transfer, the transport mean free path, λ_{tr} , therefore, significantly exceeds the inelastic mean free path λ_i (typically by an order of magnitude or even more²²), implying that the scattering parameter χ ,

$$\chi = \frac{\lambda_i}{\lambda_{tr}},$$

is significantly smaller than unity. This quantity is related to the single scattering albedo $\omega = \chi/(1 + \chi)$ and is an alternative characteristic parameter indicating the influence of elastic scattering. From Fig. 7 in Ref. 22, it is seen that the value of the scattering parameter for light elements is significantly smaller than unity for energies above 100 eV. Then, the influence of elastic scattering on peak intensity ratios of organic materials is expected to be negligible.

In summary, the above example makes it clear that comparing experimental peak intensities of such reference materials with SESSA simulations can provide the spectrometer transmission function.

It should be emphasized that SESSA can perform such simulations for instruments with an arbitrary geometrical configuration. As the experimental configuration can strongly influence relative peak areas, in particular, for high energies where nondipolar terms in the photoionization cross section come into play, or for polarized x rays (see also Sec. III D), the use of SESSA may be advantageous in such cases.

D. Simulation of the inelastic background for hard x rays with and without polarization

Since the databases for the physical quantities in SESSA by default cover the energy range between 50 eV and 30 keV, simulations for hard x-ray photoelectron spectroscopy can be conveniently performed. An example of such simulations is given in Fig. 8(a), which compares SESSA results with the experimental spectrum of a sample consisting of a 52 nm Al overlayer covering an Si substrate which was irradiated by photons with an energy of $h\nu = 7936$ eV.⁴⁹

A remarkable feature of the overlayer and substrate spectral shape is the occurrence of multiple plasmons, their intensity decaying with increasing binding energy (decreasing kinetic energy or increasing energy loss) for the overlayer signal [Fig. 8(a)], while the opposite is observed for the substrate signal [Fig. 8(b)]. Note that the plasmon energies in the substrate signal can be unequivocally attributed to a plasmon in Al, i.e., in the overlayer. These features can be qualitatively understood by considering the fact that, for such high energies, the photoelectron trajectories are rectilinear to a good approximation. For rectilinear motion, the distribution of path lengths for those trajectories that contribute to the signal is equal to the distribution in-depth of the emitting atoms, i.e., the path length distribution is identical to the compositional depth profile, while for weak elastic scattering, merely a similarity between these quantities is expected. This fact implies that the traveled path lengths are very different for the overlayer and substrate signals. The number of inelastic-scattering processes n , which in the present case essentially equals the number of excited plasmons, increases with the traveled path length s as^{22,28}

$$W_n(s) = \left(\frac{s}{\lambda}\right)^n \frac{\exp(-s/\lambda)}{n!}. \quad (8)$$

The number of n -fold plasmon excitation C_n can then be expressed in terms of the distribution of path lengths $Q(s)$ as

$$C_n = \int_0^\infty Q(s) W_n(s) ds. \quad (9)$$

As usual, the quantities C_n represent the contribution of the spectrum of the n -fold inelastically scattered electrons, the partial intensities¹⁵ which for the simple case of an overlayer on a substrate, of concern here, are found by (partial) integration of Eq. (9) as

$$C_n = \{W_n(z_1) - W_n(z_2)\} + C_{n-1}, \quad (10)$$

where for the overlayer, $z_1 = 0$ and $z_2 = d$, while for the substrate partial intensities, one has $z_1 = d$ and $z_2 = \infty$, and it is assumed

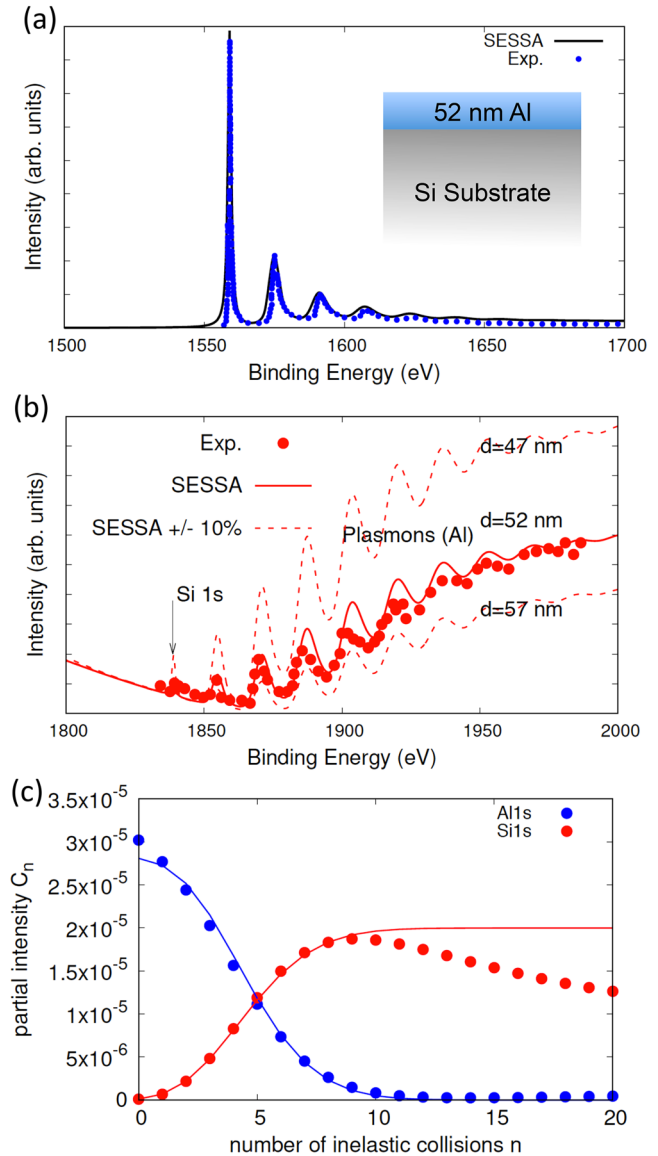


FIG. 8. Hard x-ray photoelectron spectra of a 52 nm Al overlayer on an Si substrate excited with polarized x rays with $h\nu = 7936$ eV (Ref. 49): (a) comparison of the experimental spectrum of the Al 1s overlayer signal with SESSA simulation; (b) same as (a) for the Si 1s-signal; and (c) partial intensities for overlayer and substrate signal. Data points: SESSA and solid lines: Eq. (10).

for simplicity that the IMFPs in the substrate and overlayer are identical.

Figure 8(c) compares the Al 1s and Si 1s partial intensities calculated by SESSA with the simple model [Eq. (10)] discussed above. The agreement is reasonable, except for large values of $n > 10$ (large depths), where the influence of elastic-electron scattering is more important and for $n \sim 0$ (small depths), which is related to the initial source angular distribution (see also further below).

Overall, the comparison in Fig. 8 demonstrates the ability of SESSA to predict relative intensities and spectral shapes. In particular, the shape and intensity of the inelastic background accompanying the Si 1s peak [in Fig. 8(b)] reproduces the experimental data quite well, while similar simulations for Al film thicknesses 10% above and below the nominal specimen thickness yield distinctly different shapes of the inelastic background. This result not only gives confidence in the reliability of the databases in SESSA but also suggests a simple way to measure film thicknesses using the spectral shape of the inelastic background.

Finally, note again that the weak Si 1s peak of the buried layer in Fig. 8(b) is accompanied by a series of (multiple) plasmon loss peaks whose energy separation corresponds exactly to the plasmon loss in Al. These energy losses (≈ 15 eV) are distinctly different from the plasmon energy loss in Si (≈ 16 eV). This result implies that a comparatively large number of secondary electrons created as a result of an interaction with the incoming beam in the buried layer are generated later when the photoelectron loses energy during its passage through the overlayer. The plasmons excited in this way can decay and transfer their energy and momentum to a solid-state electron, which is emitted as a secondary electron if its energy is large enough to overcome the surface barrier.^{50–54} Since the momentum transferred to the secondary electron is small for high-energy electrons, its point of escape will be in the vicinity of the Si atom that emitted the photoelectron. This result explains the good lateral resolution of the photoelectron emission microscope for buried layers, which was the original purpose of this experiment.⁴⁹

At sufficiently high energies, the momentum of the photon is no longer negligible and the dipole approximation (DA) is no

longer a good approximation. Within the DA, the angular distribution of emitted photoelectrons is symmetric with respect to a plane perpendicular to the photon propagation direction, which is equivalent to stating that the photon momentum can be neglected for the overall kinematics of the interaction (see Fig. 9). For photon energies greater than about 2 keV when the nondipolar (NDA) terms in the photoelectric cross section become important, the photoelectron angular distribution exhibits an asymmetry, which in essence represents momentum conservation.^{37,55,56}

A further experimental factor determining the source angular distribution is the polarization state of the beam. For unpolarized or circularly polarized light, the angular distribution assumes a donutlike shape, while for linearly polarized light, it assumes the typical dipole shape (see Fig. 9). A convenient formulation of the effects of the polarization state and nondipolar terms in the photoelectric cross section is given in Ref. 57, which is implemented in SESSA. Together with adequate values of the dipolar and nondipolar asymmetry parameters incorporated in the SESSA databases,^{58–61} SESSA provides a realistic description of the initial photoelectron angular distribution at the source.

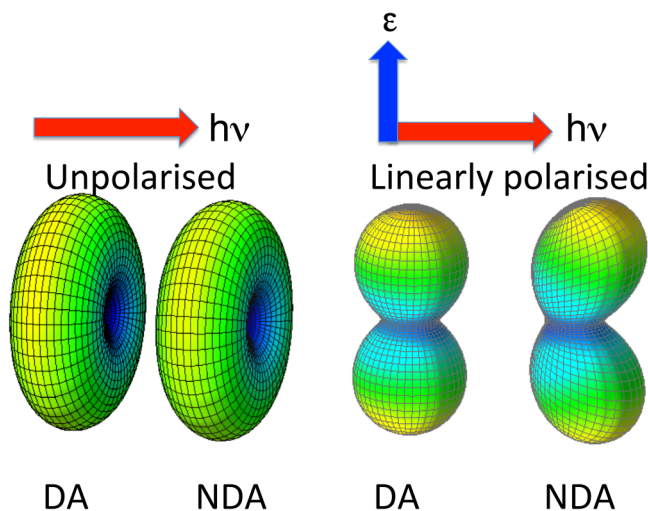


FIG. 9. Schematic illustration of the effect of nondipolar terms [nondipolar approximation (NDA) opposed to dipole approximation (DA)] as well as the effect of (linear) polarization of the photon beam on the angular dependence of the photoionization cross section, after (Ref. 55). The arrow labeled $h\nu$ indicates the direction of propagation of the light, and ϵ is the polarization vector. The angular shape of the cross section for circularly polarized light is identical to the unpolarized case (see text).

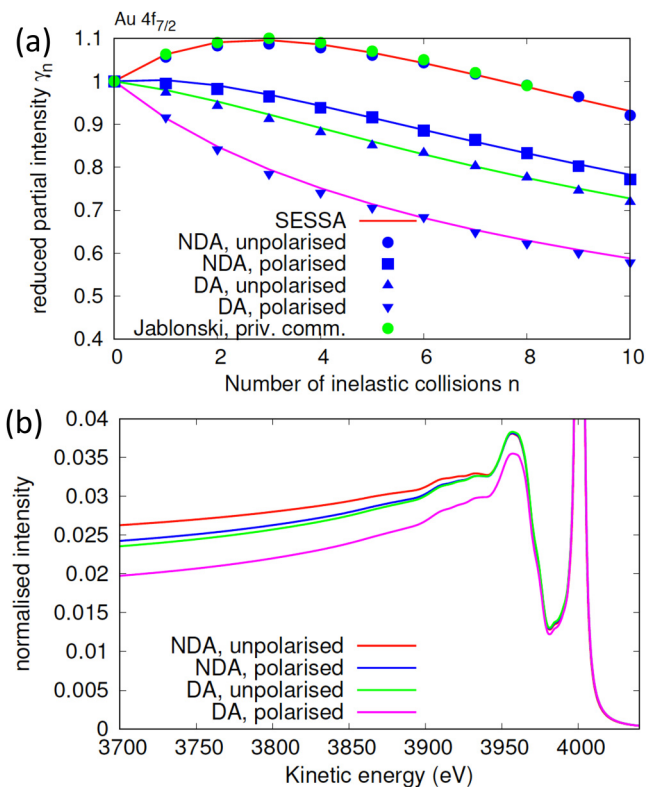


FIG. 10. (a) Reduced partial intensities of the Au $4f_{7/2}$ peak excited with photons with $h\nu = 4085$ eV; comparison of SESSA (solid lines) with results by Novák *et al.* (Ref. 55) (squares and triangles, blue) and Jablonski (circles, green) (Ref. 37). (b) Photoelectron spectra simulated with SESSA corresponding to the partial intensities shown in (a), normalized by the photopeak intensity.

It is well known that the angular distribution of photoelectrons at their source not only has implications for the photoelectron angular distribution measured in vacuum³⁷ but also influences the shape of the inelastic background accompanying the photopeak.²² As discussed above, the inelastic background is governed by the distribution of path lengths taken by the photoelectrons on their way from the source to the surface and, in the presence of elastic scattering, this is clearly influenced by the source angular distribution.

In Figs. 10(a) and 10(b), the influence of nondipolar terms in the photoelectron ionization cross section as well as the polarization state of the incoming light on the partial intensities is illustrated for an Au sample irradiated with photons with an energy of $h\nu = 4085$ eV and compared with results by Novák *et al.*⁵⁵ and Jablonski,³⁷ yielding excellent agreement. The sequence of partial intensities is clearly influenced by the source angular distribution, leading to significantly different spectral shapes, as shown in Fig. 10(b).

E. Analysis of core-shell nanoparticles

Since the chemical characterization of core-shell nanoparticles (CSNPs) is rapidly gaining importance in nanotechnology, analytical techniques originally developed for catalysis⁶² and based on XPS measurements are being adopted for NP research. The present version of the SESSA software V2.2 (Ref. 12) is able to simulate XPS spectra for surfaces with certain nanomorphologies such as core-shell particles, multishell particles, and lines and islands on layered planar surfaces and has been successfully employed in several applications.^{63–74} In particular, SESSA has been used to quantify shell thicknesses based on XPS measurements. Other methods to quantify shell thicknesses of CSNPs have been proposed in the literature, such as the “ T_{NP} ”-formula by Shard.⁷⁵ This is a simple

predictive formula allowing one to calibrate shell thicknesses from measured core/shell XPS-intensity ratios, assuming the core radius to be known. The formula was empirically derived by parameterization of a large set of calculations for core shell intensity ratios in which elastic scattering was neglected. A further method for quantifying shell thicknesses is the infinitesimal column model,⁷⁶ which is also based on the rectilinear motion model and requires a more involved numerical procedure. SESSA has been used to investigate the range of validity of these approaches⁶⁶ and has been instrumental in the INNANOPART (Ref. 77) project aimed at developing procedures for accurate characterization of the chemistry of shell materials in CSNPs. A recent publication⁷⁸ summarizes a Technical Report⁷⁹ from the International Organization for Standardization with guidelines and recommendations on quantifying XPS data for analysis of nanoparticles with coatings.

Here, we present a result from a study on the limitations imposed by making the single-sphere approximation mentioned above on the interpretation of XPS intensities from nanoparticles.⁷¹ In heterogeneous catalysis, the catalyst may be assumed to be a morphological aggregate resembling a powder consisting of core-shell nanoparticles. Models to quantitatively interpret XPS signal intensities of core-shell particles have been developed.^{62,75,80–83} The single-sphere approximation is generally assumed to describe the relative XPS intensities for a random aggregate of many nanoparticles forming a powder. With this approximation, the relative photoelectron intensities are assumed to be equivalent to those of a single spherical core-shell particle.^{62,80} The single-sphere approximation implies that the angular distribution of photoelectrons for powders is essentially isotropic since a sphere looks the same irrespective of the direction from which it is observed.

To investigate the validity of the single-sphere assumption, the polar angular distribution of XPS peak intensities has been simulated for an aggregate of core-shell nanoparticles, as shown in

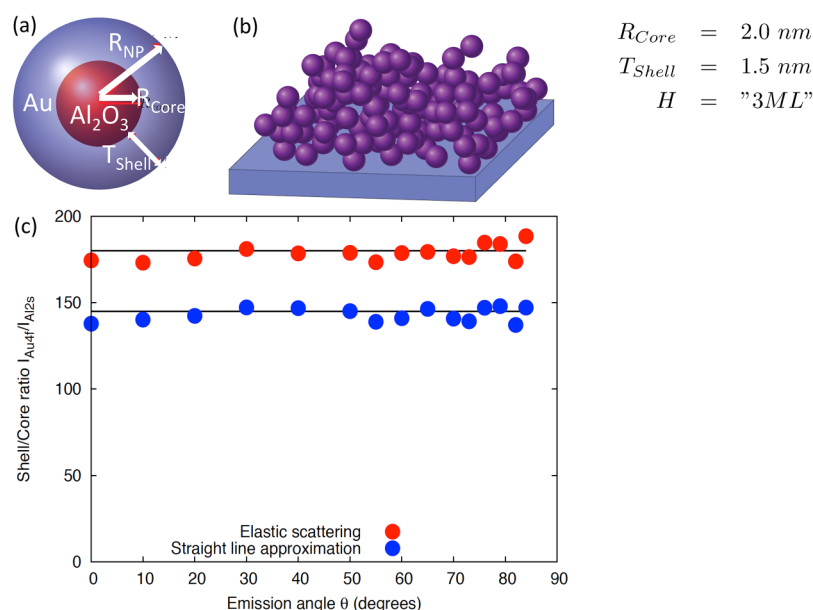


FIG. 11. Test of the powder-hypothesis of nanoparticle analysis with XPS. (a) Schematic illustration of nanoparticle structure and (b) powder structure consisting of particles displayed in (a). Angular distribution of peak intensity ratios for the structure shown in (b) with account for elastic scattering (data points labeled “Elastic scattering”) and without elastic scattering (data points labeled “Straight line approximation”) (see text).

Fig. 11(b). This system consisted of Au/Al₂O₃ core-shell NPs ($R_{\text{Al}_2\text{O}_3, \text{Core}} = 2.0$ nm, $R_{\text{Au, Shell}} = 1.5$ nm). These simulations were carried out with a developmental version of SESSA.

The points labeled “Elastic scattering” in Fig. 11(c) represent the Au4f_{7/2}-Al2s intensity ratio as a function of the (off-normal) polar emission angle θ of a single core-shell NP when elastic scattering is accounted for, and the points labeled “Straight line approximation” show the corresponding result in the straight-line approximation when elastic scattering is “turned off” in the simulations. The featureless angular distributions for the intensity ratio are expected both for the straight-line approximation and the more physically realistic case when elastic scattering is accounted for since a single-sphere looks identical irrespective of the direction of observation. This result remains true for different types of opacity of the spheres for the signal electrons, i.e., moving along straight lines or along zig-zag-shaped trajectories. In the latter case, the path length elongation along the penetration depth into the NP reduces the core signal, giving rise to a somewhat larger shell-core intensity ratio. Therefore, the core-shell intensity ratio changes significantly for the considered system consisting of materials with a high atomic number for which elastic-electron scattering is known to have a significant effect on the photoelectron intensities.²²

IV. CONCLUSIONS

In summary, the functionality of SESSA has been revisited and two new features, which have recently been added to the newest version (SESSA V2.2) of the software have been introduced. The latter concern the simulation of surface excitations and an effective approach to account for the energy dependence of the interaction characteristics for photoelectrons. Some functionalities of SESSA have been discussed on the basis of various applications, including overlayer measurements to determine the effective electron attenuation length, quantitative analysis of impurities in multilayer materials, analysis of ionic liquids, the influence of nondipolar effects for photon energies above a few keV, and analysis of nanoparticles by means of photoelectron spectroscopy.

DATA AVAILABILITY

The data that support the findings of this study are available from the corresponding author upon reasonable request.

REFERENCES

- ¹A. Keqi *et al.*, *Phys. Rev. B* **97**, 155149 (2018).
- ²G. Conti *et al.*, *APL Mater.* **6**, 058101 (2018).
- ³G. Singh-Bhalla *et al.*, *Phys. Rev. Mater.* **2**, 112001 (2018).
- ⁴C. S. Conlon *et al.*, *J. Appl. Phys.* **126**, 075305 (2019).
- ⁵W. S. M. Werner, W. Smekal, and C. J. Powell, *NIST Database for Simulation of Electron Spectra for Surface Analysis SRD100, Version 1.0* (National Institute of Standards and Technology, Gaithersburg, MD, 2005).
- ⁶W. Smekal, W. S. M. Werner, and C. J. Powell, *Surf. Interface Anal.* **37**, 1059 (2005).
- ⁷W. S. M. Werner, W. Smekal, and C. J. Powell, *Simulation of Electron Spectra for Surface Analysis (SESSA), Version 2.2.0, User's Guide, NIST NSRDS 100* (National Institute of Standards and Technology, Gaithersburg, MD, 2021).
- ⁸G. H. Major, T. G. Arval, D. S. D. I. Patel, T. Roychowdhury, A. J. Barlow, P. J. Pigram, M. Greiner, V. Fernandez, and A. H.-G. M. R. Linford, *Surf. Interface Anal.* **53**, 689 (2021).

- ⁹W. H. Gries and W. S. M. Werner, *Surf. Interface Anal.* **16**, 149 (1990).
- ¹⁰W. S. M. Werner, W. Smekal, and C. J. Powell, *NIST Database for Simulation of Electron Spectra for Surface Analysis SRD100, Version 2.0* (National Institute of Standards and Technology, Gaithersburg, MD, 2014).
- ¹¹J. Almansa, F. Salvat-Pujol, G. Diaz-Londono, A. Carnicer, A. M. Lallena, and F. Salvat, *Comput. Phys. Commun.* **199**, 102 (2016).
- ¹²W. S. M. Werner, W. Smekal, and C. J. Powell, *NIST Database for Simulation of Electron Spectra for Surface Analysis SRD100, Version 2.2* (National Institute of Standards and Technology, Gaithersburg, MD, 2021).
- ¹³W. S. M. Werner, M. Novak, F. Salvat-Pujol, J. Zemek, and P. Jiricek, *Phys. Rev. Lett.* **110**, 086110 (2013).
- ¹⁴W. S. M. Werner, W. Smekal, C. Tomastik, and H. Störi, *Surf. Sci.* **486**, L461 (2001).
- ¹⁵ISO 18115-1, *Surface Chemical Analysis Vocabulary Part 1, General Terms and Terms Used in Spectroscopy* (International Organization for Standardization, Geneva, 2010).
- ¹⁶W. S. M. Werner, *Surf. Interface Anal.* **35**, 347 (2003).
- ¹⁷W. S. M. Werner, *Surf. Sci.* **526**, L159 (2003).
- ¹⁸R. Oswald, “Numerische untersuchung der elastischen streuung von elektronen an atomen und ihrer rückstreuung an oberflächen amorpher substanzen im energiebereich unter 2000 eV,” Ph.D. thesis (Eberhard-Karls-Universität Tübingen, 1992).
- ¹⁹E. A. Stern and R. A. Ferrell, *Phys. Rev.* **120**, 130 (1960).
- ²⁰Y. F. Chen, *Surf. Sci.* **519**, 115 (2002).
- ²¹R. H. Ritchie, *Phys. Rev.* **106**, 874 (1957).
- ²²W. S. M. Werner, *Surf. Interface Anal.* **31**, 141 (2001).
- ²³Z.-J. Ding, “Fundamental studies on the interactions of kV electrons with solids for application to electron spectroscopies,” Ph.D. thesis (Osaka University, 1990).
- ²⁴K. M. Case and P. F. Zweifel, *Linear Transport Theory* (Addison-Wesley, Reading, MA, 1967).
- ²⁵M. Hronek, “Simulation of x-ray photoelectron spectra beyond the quasi-elastic approximation: Application to nanoparticle analysis,” Master's thesis (Vienna University of Technology, 2019).
- ²⁶B. Davison, *Neutron Transport Theory* (Oxford University, Oxford, 1955).
- ²⁷I. S. Tilinin and W. S. M. Werner, *Phys. Rev. B* **46**, 13739 (1992).
- ²⁸W. S. M. Werner, *Phys. Rev. B* **55**, 14925 (1997).
- ²⁹C. J. Powell, *J. Electron Spectrosc. Relat. Phenom.* **44**, 29 (1974).
- ³⁰C. R. Brundle, *J. Vac. Sci. Technol.* **11**, 212 (1974).
- ³¹I. Lindau and W. E. Spicer, *J. Electron Spectrosc. Relat. Phenom.* **3**, 409 (1974).
- ³²M. P. Seah and W. A. Dench, *Surf. Interface Anal.* **1**, 2 (1979).
- ³³A. Jablonski and C. J. Powell, *J. Phys. Chem. Ref. Data* **49**, 033102 (2020).
- ³⁴J. Rubio-Zuazo and G. Castro, *J. Electron Spectrosc. Relat. Phenom.* **184**, 384 (2011).
- ³⁵C. J. Powell and A. Jablonski, *J. Electron Spectrosc. Relat. Phenom.* **236**, 27 (2019).
- ³⁶S. Tanuma, C. J. Powell, and D. R. Penn, *Surf. Interface Anal.* **43**, 689 (2011).
- ³⁷A. Jablonski, *Surf. Sci.* **667**, 121 (2018).
- ³⁸C. J. Powell, *J. Vac. Sci. Technol. A* **38**, 023209 (2020).
- ³⁹C. J. Powell, *J. Vac. Sci. Technol. A* **38**, 057001 (2020).
- ⁴⁰C. J. Powell, *Surf. Interface Anal.* **7**, 256 (1985).
- ⁴¹C. Argile and G. E. Rhead, *Surf. Sci. Rep.* **10**, 277 (1989).
- ⁴²A. Barbier, *Surf. Sci.* **406**, 69 (1998).
- ⁴³S. Tougaard, *J. Vac. Sci. Technol. A* **39**, 011201 (2021).
- ⁴⁴N. S. Faradzhev, S. B. Hill, and C. J. Powell, *Surf. Interface Anal.* **49**, 1214 (2017).
- ⁴⁵T. E. Madey, N. S. Faradzhev, B. V. Yakshinsky, and N. V. Edwards, *Appl. Surf. Sci.* **253**, 1691 (2006).
- ⁴⁶M. Holzweber, A. Lippitz, R. Hesse, R. Denecke, W. S. Werner, and W. E. Unger, *J. Electron Spectrosc. Relat. Phenom.* **233**, 51 (2019).
- ⁴⁷R. Hesse, P. Streubel, and R. Szargan, *Surf. Interface Anal.* **37**, 589 (2005).
- ⁴⁸Certain commercial instruments and software are identified to specify experimental measurement conditions and methods of data analysis. These

identifications are not intended as endorsements of these products by the national institute of standards and technology nor are they intended to imply that they are the most suitable products for the applications.

- ⁴⁹T. Kinoshita *et al.*, *Surf. Sci.* **601**, 4754 (2007).
- ⁵⁰W. S. M. Werner, F. Salvat-Pujol, A. Bellissimo, R. Khalid, W. Smekal, M. Novak, A. Ruocco, and G. Stefani, *Phys. Rev. B* **88**, 201407 (2013).
- ⁵¹W. S. M. Werner, W. Smekal, H. Winter, A. Ruocco, F. Offi, S. Iacobucci, and G. Stefani, *Phys. Rev. B* **78**, 233403 (2008).
- ⁵²W. S. M. Werner, V. Astašauskas, P. Ziegler, A. Bellissimo, L. Linhart, and F. Libisch, *Phys. Rev. Lett.* **125**, 196603 (2020).
- ⁵³O. Y. Ridzel, V. Astašauskas, and W. S. M. Werner, *J. Electron Spectrosc. Relat. Phenom.* **241**, 146824 (2020).
- ⁵⁴A. Bellissimo, G.-M. Pierantozzi, A. Ruocco, G. Stefani, O. Y. Ridzel, V. Astašauskas, W. S. M. Werner, and M. Taborelli, *J. Electron Spectrosc. Relat. Phenom.* **241**, 146883 (2020).
- ⁵⁵M. Novák, N. Pauly, and A. Dubus, *J. Electron Spectrosc. Relat. Phenom.* **185**, 4 (2012).
- ⁵⁶W. S. M. Werner, W. Smekal, T. Hisch, J. Himmelsbach, and C. J. Powell, *J. Electron Spectrosc. Relat. Phenom.* **190**, 137 (2013).
- ⁵⁷P. S. Shaw, U. Arp, and S. H. Southworth, *Phys. Rev. A* **54**, 1463 (1996).
- ⁵⁸R. F. Reilman, A. Msezane, and S. T. Manson, *J. Electron Spectrosc. Relat. Phenom.* **8**, 289 (1976).
- ⁵⁹J. J. Yeh and I. Lindau, *At. Data Nucl. Data Tables* **32**, 1 (1985).
- ⁶⁰M. B. Trzhaskoskaya, V. I. Nefedov, and V. G. Yarzhevsky, *At. Data Nucl. Data Tables* **77**, 97 (2001).
- ⁶¹M. B. Trzhaskoskaya, V. I. Nefedov, and V. G. Yarzhevsky, *At. Data Nucl. Data Tables* **82**, 257 (2003).
- ⁶²H. P. C. E. Kuipers, H. C. E. van Leuven, and W. M. Visser, *Surf. Interface Anal.* **8**, 235 (1986).
- ⁶³C. Powell, W. Werner, A. Shard, and D. Castner, *J. Phys. Chem. C* **120**, 22730 (2016).
- ⁶⁴C. J. Powell, M. Chudzicki, W. S. M. Werner, and W. Smekal, *J. Vac. Sci. Technol. A* **33**, 05E113 (2015).
- ⁶⁵C. J. Powell, W. S. M. Werner, and W. Smekal, *J. Vac. Sci. Technol. A* **32**, 050603 (2014).
- ⁶⁶M. Chudzicki, W. S. Werner, A. G. Shard, Y. C. Wang, D. G. Castner, and C. J. Powell, *J. Phys. Chem. C* **119**, 17687 (2015).
- ⁶⁷C. J. Powell, S. Tougaard, W. S. M. Werner, and W. Smekal, *J. Vac. Sci. Technol. A* **31**, 021402 (2013).
- ⁶⁸C. J. Powell, W. S. Werner, H. Kalbe, A. G. Shard, and D. G. Castner, *J. Phys. Chem. C* **122**, 4073 (2018).
- ⁶⁹N. Belsey *et al.*, *J. Phys. Chem. C* **120**, 24070 (2016).
- ⁷⁰M. Chudzicki, W. S. M. Werner, A. G. Shard, Y.-C. Wang, D. G. Castner, and C. J. Powell, *J. Phys. Chem. C* **120**, 2484 (2016).
- ⁷¹W. S. M. Werner, M. Chudzicki, W. Smekal, and C. J. Powell, *Appl. Phys. Lett.* **104**, 243106 (2014).
- ⁷²A. Müller *et al.*, *J. Phys. Chem. C* **123**, 029765 (2019).
- ⁷³A. Müller, T. Krah, J. Radnik, A. Wagner, C. Kreyenschulte, W. S. Werner, B. Ritter, E. Kemnitz, and W. E. Unger, *Surf. Interface Anal.* **53**, 494 (2021).
- ⁷⁴D. J. Cant, C. Minelli, K. Sparnacci, A. Müller, H. Kalbe, M. Stöger-Pollach, W. E. Unger, W. S. Werner, and A. G. Shard, *J. Phys. Chem. C* **124**, 011200 (2020).
- ⁷⁵A. G. Shard, *J. Phys. Chem. C* **116**, 016806 (2012).
- ⁷⁶H. Kalbe, S. Rades, and W. E. S. Unger, *J. Electron Spectrosc. Relat. Phenom.* **212**, 34 (2016).
- ⁷⁷Innanopart euramet empir project, see <http://empir.npl.co.uk/innanopart/>.
- ⁷⁸D. J. H. Cant, A. Müller, C. A. Clifford, W. E. S. Unger, and A. G. Shard, *Surf. Interface Anal.* (published online) (2021).
- ⁷⁹International Organization for Standardization, *ISO/TR 23713: 2021 Surface Chemical Analysis -Electron Spectroscopies—Measurement of the Thickness and Composition of Nanoparticle Coatings* (International Organization for Standardization, Geneva, 2021).
- ⁸⁰A. Frydman, D. G. Castner, M. Schmal, and C. T. Campbell, *J. Catal.* **83**, 866 (2011).
- ⁸¹A. Rafati, R. ter Veen, and D. G. Castner, *Surf. Interface Anal.* **157**, 1737 (2013).
- ⁸²S. Techane, L. J. Gamble, and D. G. Castner, *J. Phys. Chem. C* **115**, 9432 (2011).
- ⁸³S. Techane, D. R. Baer, and D. G. Castner, *Anal. Chem.* **83**, 6704 (2011).